

Supplementary Material

for

Can AFM be used to measure absolute values of the Young's modulus of nanocomposite materials down to the nanoscale?

Y. Liu^{a,b,f}, I. Sokolov^{a,c,d,*}, M.E. Dokukin^{a,e}, Y. Xiong^b, P. Peng^b

a. Department of Mechanical Engineering, Tufts University, Medford, MA, USA.

b. Guangzhou Institute of Geochemistry, Chinese Academy of Sciences, Guangzhou, China.

c. Department of Biomedical Engineering, Tufts University, Medford, MA, USA.

d. Department of Physics, Tufts University, Medford, MA, USA

e. Sarov Physical and Technical Institute, National Research Nuclear University MEPhI, Sarov, Russian Federation

f. Guangzhou Marine Geological Survey, China Geological Survey, Guangzhou, China

* Corresponding author: igor.sokolov@tufts.edu

1. The algorithm to use only relatively flat area of the sample to calculate the effective Young's modulus

Gradient Norm angle is used to estimate the flatness of the sample being indented. This value is calculated in SPIP software automatically. It can be found using any other software as follows. The Gradient Norm is equal to the angle of the local normal vector minus 90 degrees. It is zero for a flat surface. For high slopes the angle may approach 90 degrees. The way the angle θ of the normal vector N calculated is as follows. For a point $P_{0,0}$, four normal vectors are found based using four triangles around $P_{0,0}$:

$$P_{0,0} = (x, y, z(x, y))$$

$$P_{1,0} = (x + 1, y, z(x + 1, y))$$

$$P_{0,1} = (x, y + 1, z(x, y + 1))$$

$$P_{-1,0} = (x - 1, y, z(x - 1, y))$$

$$P_{0,-1} = (x, y - 1, z(x, y - 1)).$$

Then,

$$N_1 = \text{Normal vector of Triangle } P_{0,0}, P_{1,0}, P_{0,1}$$

$$N_2 = \text{Normal vector of Triangle } P_{0,0}, P_{0,-1}, P_{-1,0}$$

$$N_3 = \text{Normal vector of Triangle } P_{0,0}, P_{-1,0}, P_{0,1}$$

$$N_4 = \text{Normal vector of Triangle } P_{0,0}, P_{0,-1}, P_{1,0}$$

$$N_a = (N_1 + N_2 + N_3 + N_4)/4$$

$$N = N_a / |N_a|$$

$$\sin \varphi = \sqrt{N_x^2 + N_y^2}.$$

And finally, the gradient norm angle is calculated using the following formula:

$$\theta = \left| 90 - \frac{180}{\pi \cos^{-1}(\sin \varphi)} \right|.$$

2. Roughness of the shale sample measured by AFM

Although the sample preparation was done rather carefully, the residual roughness still exists. Fig. S1 shows a typical surface topography (Fig. S1 a) and a cross-section of the shale sample (Fig. S1 b) (the image was obtained using a regular (sharp) AFM probe). The analysis shows typically less than 1 nm peak-to-valley roughness at the scale of the AFM probe contact (about 80 nm, see the Results section for detail).

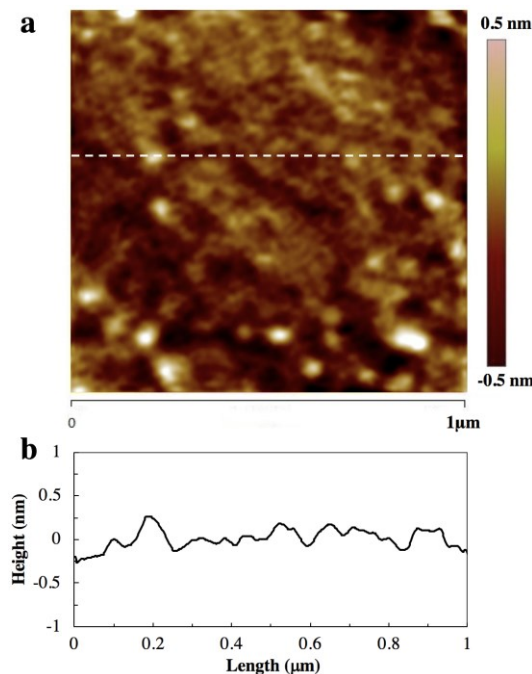
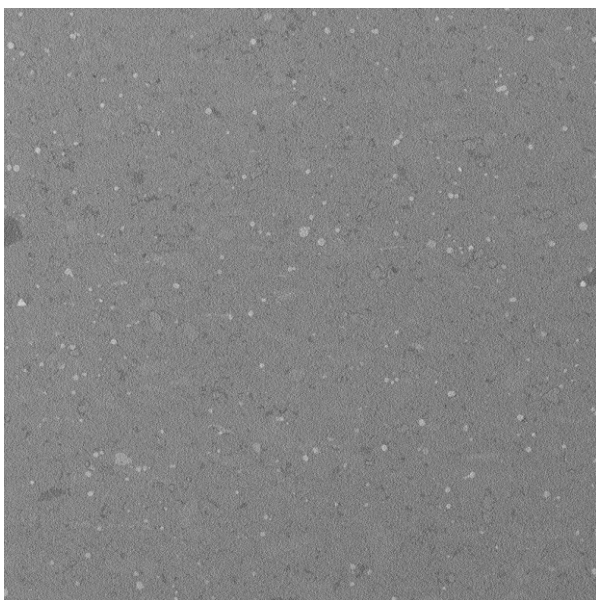


Fig. S1. (a) A typical surface topography and (b) cross-section height distribution of the shale sample imaged by using a sharp AFM probe of an area of $1 \times 1 \mu\text{m}^2$. A typical less than 1 nm peak-to-valley roughness at the scale of the AFM probe contact diameter ($\sim 80 \text{ nm}$) can be seen.

3. SEM and EDS Analysis of the Shale Surface: Relative Homogeneity at Multi-Micron Scale

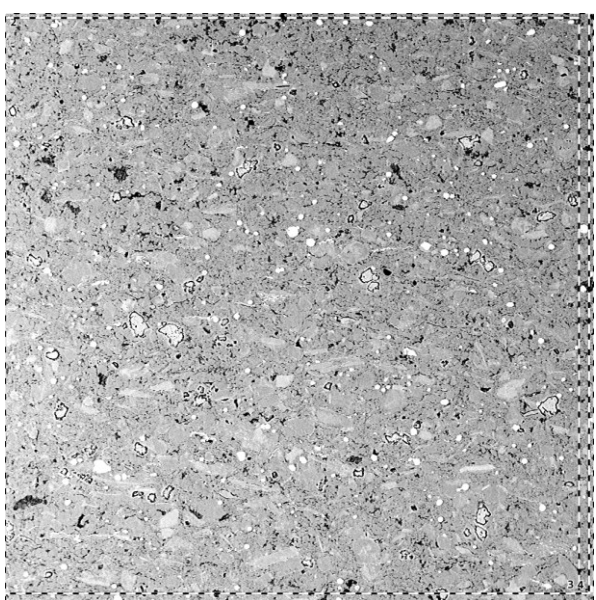
Figure S2 shows an example of the SEM image of the shale sample surface. The top row demonstrates the images obtained with 5 kV and 15 kV. A high heterogeneity is clearly seen at 15 kV, thereby demonstrating higher homogeneity near the surface. The bottom rows images shows the distribution of corresponding elements. The darker means higher concentration of the corresponding element.

5kV

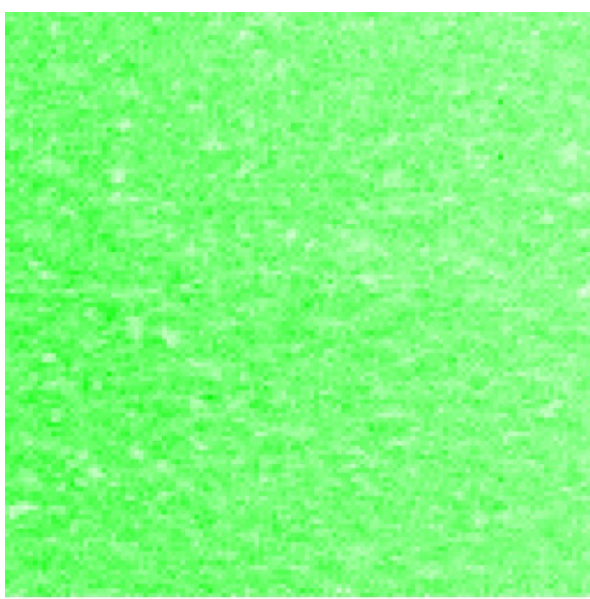


Oxygen

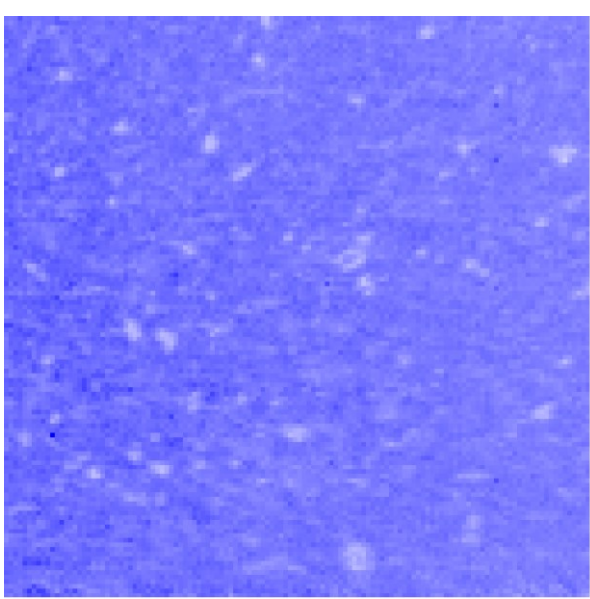
15kV



Silicon



Aluminum



Carbon

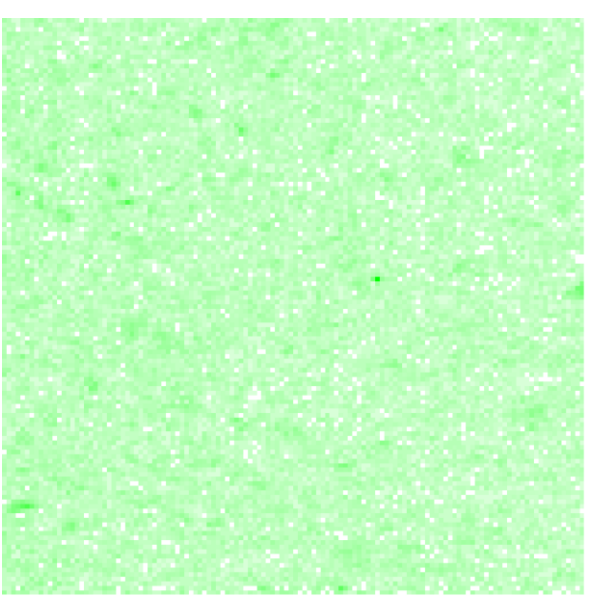
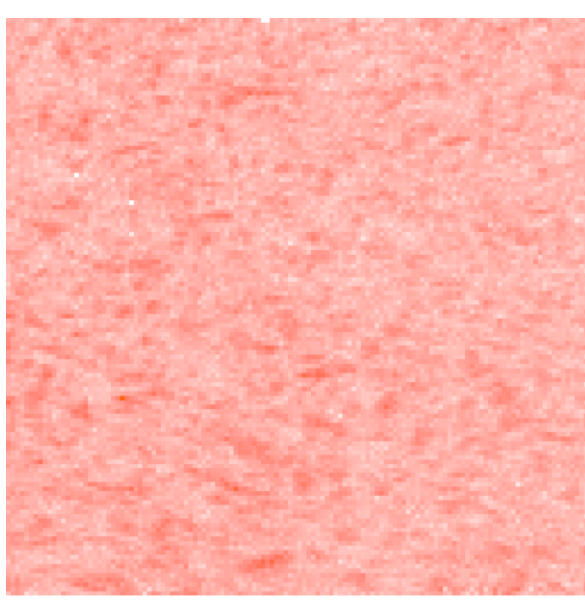


Fig. S2. A an example of the SEM image of $500 \times 500 \mu\text{m}^2$ shale sample surface. The top row demonstrates the images obtained with 5 kV and 15 kV. The bottom rows images shows the 128x128 pixel distribution of corresponding elements. The darker means higher concentration of the corresponding element.

Table S1. The results of EDS measurements of the shale sample surface shown in figure S2.

Element name	Concentration percentage	Certainty percentage	Error percentage
Oxygen	66.2	99.9	0.1
Silicon	28.8	99.9	0.1
Aluminium	3.5	99.8	0.2
Carbon	0.9	99.3	0.7

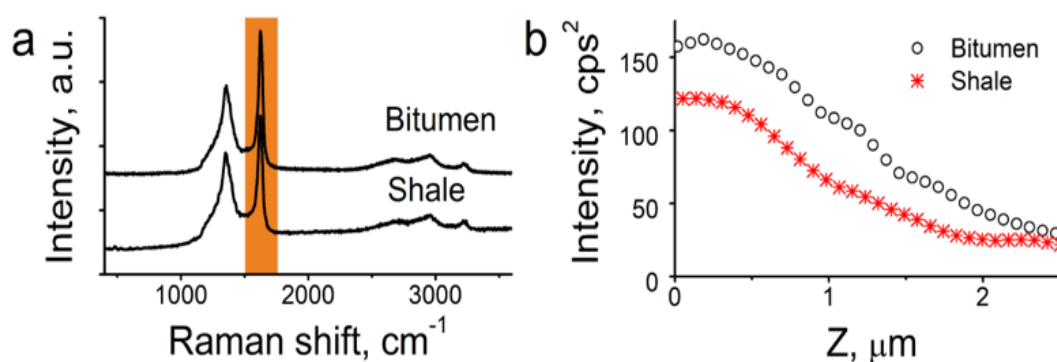


Fig. S3. Raman study of the samples. (a) Typical Raman spectra for organic matter from solid bitumen (peak 1350 cm^{-1} and peak 1600 cm^{-1}). (b) Depth profile of 1600 cm^{-1} Raman signal-averaged along the sample line shown in panels of Fig.S4.

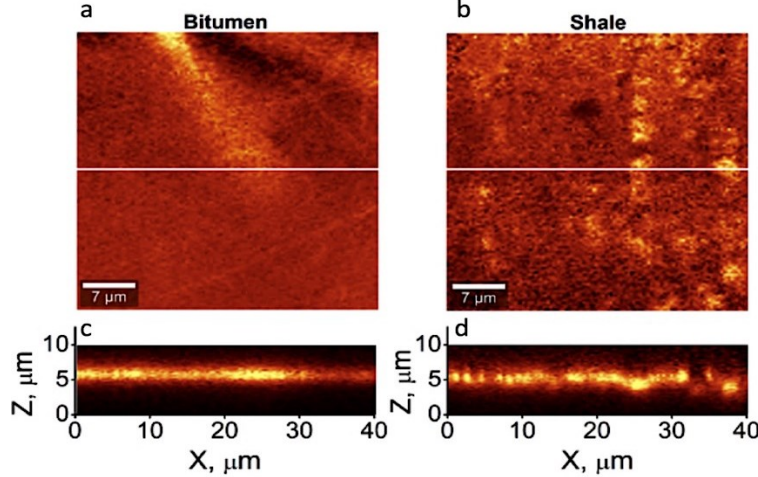


Fig. S4. Raman images of the samples (a,b) 40 $\mu\text{m} \times 40 \mu\text{m}$ maps of Raman signal at 1600 cm^{-1} obtained on the surface of (a) bitumen and (b) shale samples. (c,d) 10 μm depth distributions of 1600 cm^{-1} signal across the samples shown by solid lines in panels (a,b), respectively.

4. Finding of the reduced Young's modulus of the AFM probe

According to the manufacturer (NanoScience Solutions, Inc.), the material of the probe is reinforced silica glass. The properties of this material at the nanoscale are unknown. Therefore, we need to measure it. Specifically, we will measure the reduced modulus of the indenting probe E_{ri} , which is defined as follows

$$E_{ri} = \frac{E_i}{(1 - \nu_i^2)}, \quad (\text{S1})$$

where E_i and ν_i are the Young's modulus and Poisson's ratio of the probe.

In further calculations, we don't need to know the Young's modulus and Poisson ratio separately. Therefore, the measurements of the reduced Young's modulus is sufficient.

The reduced Young's modulus of the probe can be found when measuring the force indentation curves with respect to two known materials. Specifically, using DMT model, one has the following force – indentation dependence for each of non-material:

$$F = \frac{4}{3} E_{r1} \sqrt{R \delta^3} + F_{adh1}, \quad (\text{S2})$$

and

$$F = \frac{4}{3} E_{r2} \sqrt{R \delta^3} + F_{adh2}, \quad (\text{S3})$$

where F is the load force, R is the curvature radius of the AFM probe, δ is the indentation depth, and F_{adh} is the adhesion.

The reduced modulus of the probe – sample contact is defined as follows

$$\frac{1}{E_{r1}} = \frac{(1-v_{s1}^2)}{E_{s1}} + \frac{1}{E_{ri}} \text{ and } \frac{1}{E_{r2}} = \frac{(1-v_{s2}^2)}{E_{s2}} + \frac{1}{E_{ri}}, \text{ for samples one and two, respectively.}$$

The indentation depth can be found as $\delta = Z - Z_0 + d$, where Z is the vertical position of the sample, Z_0 is the point of contact between the AFM probe and sample, and d the deflection of the cantilever. The force can be found as a multiplication of d and the spring constant of the cantilever.

When collecting the raw AFM data, Z versus d , the equations S2 and 3 can be written as follows:

$$d \beta \Delta V = \frac{4}{3} E_{r1} \sqrt{R(Z - Z_0 + \beta \Delta V)^3} + F_{adh1}, \quad (S4)$$

$$d \beta \Delta V = \frac{4}{3} E_{r2} \sqrt{R(Z - Z_0 + \beta \Delta V)^3} + F_{adh2}, \quad (S5)$$

where β is the sensitivity of the photodetector- AFM cantilever, ΔV is the signal from the photodetector in Volts.

The system of two equations S4 and 5 is the system with respect to unknown variables, E_{ri} and the sensitivity of the photodetector, β . It is possible to find a solution for both.

In the specific application, we used the sample of amorphous silica glass ($E_{s1} = 70$ GPa and $v_{s1}=0.17$), and the sapphire calibration sample by Bruker ($E_{s2} = 360$ GPa and $v_{s2}=0.3$). The load force was limited by 8 μ N. The results of the solution of the system of two equations S4 and 5 were as follows: $\beta = 62.5 \frac{nm}{V}$, $E_{ri} = 120$ GPa.

5. Discussion of possible alteration of the sample surface due to ion milling in the supplementary materials

There is a concern that ion milling may produce unrelaxed stresses in the sample surface. We don't think it would stay long due to the presence of a soft bitumen phase, which would tend to relax those pretty quickly. Furthermore, if the stresses were there, and it influenced the mechanical properties of the sample, we would see the discrepancy between the AFM and nanoindenter measurements.

As a general note, unlike metal materials, little research has been conducted on characterizing residual stress of shale after polishing. We suppose the difficulty may be due to the high heterogeneity of shale, of which the XRD spectrum (traditionally used to calculate residual stress) is a combination of various phases, and thereby hard to figure out the changes of before and after polishing for each individual constitute. Comparatively, the heating effect during polishing has gained much attention. Among all the constitutes in shale, the organic phase is supposed to be most sensitive to the heating process during polishing. For both solid bitumen (almost the pure organic) and shale sample (with an organic matrix), the investigation on the organic phase may help figure out to what extent the heating effect could be.

So far, the impact of ion milling is still under debate. Significant sample heating (limited to a few nanometers under the surface) during milling could result in fast devolatilization of aliphatic compounds and reflectance increases in organic matter^{1, 2}, whereas it is supposed to be avoided by applying correct polishing setting³. However, the most recent work suggested this artificial effect is pronounced in immature samples ($Ro < 1.0\%$), but is minor or even absent for samples of high maturity ($Ro > 1.0\%$)⁴.

Here, maturity (Ro%) is a parameter to evaluate the optical reflectance properties of organic matter, which is positively related with the degree of aromatization in organic molecules^{5, 6}. During geologic process, hydrocarbons can be generated from organic matter in shales through a series of decomposition reactions, from which the process of maturation can be classified into three levels: immature ($Ro < 0.5\%$; onset of hydrocarbon generation), mature ($0.5 < Ro < 1.3\%$; hydrocarbon generation), and highly mature ($Ro > 1.3\%$; oil cracks into gas)⁷.

The solid bitumen and shale samples used in this study are over mature with extremely high maturities, which are 3.68% and 2.0%, respectively. Considering the extremely high maturities of organic matter used in this study, the samples are not that susceptible to the polishing process, and may barely exhibit artificially-induced compositional changes, as well as the corresponding mechanical alternation.

Supplementary references

1. H. Sanei and O. H. Ardakani, *International Journal of Coal Geology*, 2016, **163**, S0166516216302221.
2. I. Arango and B. J. Katz, presented in part at the AAPG Annual Convention and Exhibition, Houston, Texas, 2017.
3. A. Grobe, J. Schmatz, R. Littke, J. Klaver and J. L. Urai, *International Journal of Coal Geology*, 2017, **180**, 113-121.
4. M. Mastalerz and J. Schieber, *International Journal of Coal Geology*, 2017, **183**, 110-119.
5. M. Miller, C. Bobko, M. Vandamme and F.-J. Ulm, *Cement and Concrete Research*, 2008, **38**, 467-476.
6. L. Chen, A. Ahadi, J. Zhou and J.-E. Ståhl, *Procedia CIRP*, 2013, **8**, 334-339.
7. B. Tissot, B. Durand, J. Espitalie and A. Combaz, *AAPG Bulletin*, 1974, **58**, 499-506.